Advances in Nano Research, *Vol. 14, No.1 (2023) 27-43*
https://doi.org/10.12989/anr.2023.14.1.027

Vibration based energy harvesting performance of magneto-electro-elastic beams reinforced with carbon nanotubes

Arjun Siddharth Mangalasseri[1], Vinyas Mahesh*[2], Sriram Mukunda[3], Vishwas Mahesh[1,4], Sathiskumar A Ponnusami[2], Dineshkumar Harursampath[1], Abdelouahed Tounsi[5,6,7]

[1]*Department of Aerospace Engineering, Indian Institute of Science (IISc), Bangalore – 560012, India*
[2]*Department of Engineering, City, University of London, London, EC1V 0HB, United Kingdom*
[3]*Department of Mechanical Engineering, Nitte Meenakshi Institute of Technology, Bangalore-560064, India*
[4]*Department of Industrial Engineering and Management, Siddaganga Institute of Technology, Tumkur – 572103, India*
[5]*YFL (Yonsei Frontier Lab), Yonsei University, Seoul, Korea*
[6]*Department of Civil and Environmental Engineering, King Fahd University of Petroleum & Minerals, 31261 Dhahran, Eastern Province, Saudi Arabia*
[7]*Material and Hydrology Laboratory, University of Sidi Bel Abbes, Faculty of Technology, Civil Engineering Department, Algeria*

(*Received January 13, 2022, Revised April 20, 2022, Accepted May 15, 2022*)

Abstract. This article investigates the energy harvesting characteristics of a magneto-electro-elastic (MEE) cantilever beam reinforced with carbon nanotubes (CNT) under transverse vibration. To this end, the well-known lumped parameter model is used to represent the coupled multiphysics problem mathematically. The proposed system consists of the MEE-CNT layer on top and an inactive substrate layer at the bottom. The substrate is considered to be made of either an isotropic or composite material. Basic laws such as Gauss's Law, Newton's Law and Faraday's Law are used to arrive at the governing equations. Surface electrodes across the beam are used to harvest the electric potential produced, together with a wound coil, for the generated magnetic potential. The influence of various distributions of the CNT and its volume fraction, substrate material, length-to-thickness ratio, and thickness ratio of substrate to MEE layer on the energy harvesting behaviour is thoroughly discussed. Further, the effect of external resistances and changes in substrate material on the response is analysed and reported. The article aims to explore smart material-based energy harvesting systems, focusing on their behaviour when reinforced with carbon nanotubes. The results of this study may lead to an improved understanding of the design and analysis of CNT-based smart structures.

Keywords: carbon nanotube; coupled response; energy harvester; magneto-electro-elastic; volume fractions

1. Introduction

Reinforcement materials are commonly used in various composites to improve the matrix material's thermal, mechanical, electrical, and other properties. These reinforcements can be in the form of particles, fibres, sheets etc. They are appropriately chosen as per the application and seek to obtain an optimum response from the material. Carbon-based materials have long been used as reinforcement materials for various applications. Graphene platelet (GPL) reinforced structures were seen in various works, exploring the influence of the GPLs on the strength, stiffness, and overall dynamic characteristics of the structure under consideration. The focus is on the reinforcement (GPL) distribution, volume fraction and geometry, and the corresponding effects of the vibrational behaviour (Zhou *et al*. 2020, Rad *et al*. 2020, Karami *et al*. 2020). An interesting article presented by Eyvazian *et al*. (2020) focused on the effect of functionally graded graphene platelets (FG-GPLs) on the free vibration characteristics of spherical shells. The natural frequencies for various boundary conditions, GPL volume fractions and FG distributions were extracted. Reinforcement by nanoparticles was seen in works such (She 2020, Motezaker and Eyvazian 2020a). Extensive numerical results based on the weight fraction, non-uniform distributions, thickness and clustering of these nanoparticles were computed and presented.

The remarkable properties exhibited by Carbon Nanotubes have led to their utilisation as reinforcements in various composite structures. Wang *et al*. (2014) provided a detailed insight into the properties and methods of fabrication of CNT reinforced composites for various biomedical applications. Enhancement of properties of composites such as Ceramic matrix composites and polymer matrix composites were discussed, and their compatibility for tissue engineering applications was brought to light. Gkikas *et al*. (2012) studied the effect of dispersion of Multi-Walled Carbon Nanotubes (MCWNTs) in an epoxy matrix using an ultrasonic mixer. The effect of the sonification process's duration, amplitude, and dispersion time on fracture toughness and stress intensity factor was investigated. The effect of agglomeration of nanotubes was discussed in Farokhian (2020) and Motezaker and Eyvazian (2020b). The results indicate that

*Corresponding author, Ph.D.,
E-mail: vinyas.mahesh@gmail.com;
Vinyas@mech.nits.ac.in

ISSN: 2287-237X (Print), 2287-2388 (Online)

applying negative voltage on the plate with infused smart layers results in an increase in frequency while the agglomeration effect of CNTs, decreases it. Musharavati *et al*. (2020) also considered the agglomeration effects of CNTs in FG-CNT plates covered by magnetic layers. The inclusion of the magnetic layer results in an increase in the frequency of the structure, and an extensive study on parameters such as CNT agglomeration, elastic medium, and geometric parameters were presented. Non-local strain gradient theory was utilised by Khazaei and Mohammadimehr (2020b) to carry out buckling and deflection analysis of a nanocomposite piezoelectric plate. Jagannatham *et al*. (2020) carried out a comprehensive review of Al-CNT alloys and composites, focusing on their tensile properties. Different fabrication processes of these composites were compared concerning the microstructure, CNT dispersion, and how these parameters affect the material's tensile properties. Chen *et al*. (2015) carried out an experimental investigation into the strengthening effects of MWCNT on Al-matrix composites. The fractures modes observed suggested good load transfer between the reinforcement and the matrix material during tensile failure. These observations resulted in an understanding of the efficiency of strengthening of MWCNTs. Tsai and Lu (2009) studied the load transfer efficiency in CNT reinforced nanocomposites. Various parameters which affect the load transfer were studied, including- layer number, inter-layer interaction and aspect ratio. Zhou *et al*. (2020) used the State-Space based Differential Quadrature Method (SS-DQM) to examine the vibration behaviour of annular and circular plates reinforced with nanocomposites (CNT). Sahmani *et al*. (2019) utilised the theories of nonlocal strain gradient and geometric nonlinearity in the exponential shear deformation theory to investigate the vibrational characteristics of axially loaded nanoplates. Halpin-Tsai modelling was used to compute the mechanical properties of the considered functionally graded porous material, which was reinforced with graphene platelets (GPLs). Ma *et al*. (2021) derived a mathematical formulation for the frequency response of graphene platelet reinforced annular plates. Yet again, the DQM method, along with the Perturbation approach (PA), was used to study the chaotic motion of the plate under harmonic excitation. It was concluded that the system's motion was barely dependent on the length to thickness ratio of the GPL, and increasing this ratio by using GPLs with lower thickness results in better frequency response. DQM was also used by Kolahdouzan *et al*. (2020) to conduct free vibration, and buckling analysis of CNT reinforced nanoplates, with a detailed study on the influence of SWCNT distributions and volume fraction on the behaviour of the plates. On the other hand, the differential cubature method (DCM) was utilised by Kolahchi (2020) to compute the frequency response of a sandwich nanocomposite plate reinforced with CNTs. Analysis of graphene reinforced structures in thermal environments was carried out in works such as (Ebrahimi *et al*. 2019, Allahkarami 2020). The distribution pattern of the reinforced graphene, along with temperature range, boundary conditions and geometric parameters, determine the overall performance of the structure. The dynamic torsional response of graphene oxide powders (GOPs) strengthened composite based nanorods was carried out by Ebrahimi *et al*. (2021b). The influence of boundary conditions such as C-F, C-C, nonlocal parameters and geometric ratios was explored and presented. Sohrabi and Nezhad (2020) used the novel meshless local Petrov-Galerkin method (MLPG) for dynamic analysis of a nanocomposite cylindrical shell. Different grading patterns and nanocomposite angles are considered while using the Radial Basis Functions (RBFs) to approximate the displacements.

Nazarenko *et al*. (2019) used an approximate approach to analyse a square plate with a hole made of a polymer reinforced with CNT. The effect of CNT distribution by volume fraction on the stress concentration was studied. Zare and Rhee (2020) combined two models for the tensile modulus of composites. The effect of several parameters on the modulus is investigated, including CNT radius, interphase thickness, and volume fraction. A precise formulation for studying wave propagation through double-curved shells reinforced with CNTs was presented by Ghassasbi *et al*. (2019). They found that the CNTs could enhance the sound insulation of the shells, and the sound transmission loss of the structure was validated through various configurations. Detailed vibration analysis of a viscoelastic plate reinforced with FG-Single Walled CNTs was presented by Khazaei and Mohammadimehr (2020a). In this work, a nonlocal strain gradient theory was used, and it was observed that the effect of the strain gradient parameter on the natural frequency is less as compared to the damping effects. The frequency also increases with an increase in strain gradient and CNT volume fraction. Similar works on buckling analysis of CNT reinforced plate and beam were presented by Zidour *et al*. (2020) and Zerrouki *et al*. (2020). Important conclusions based on the CNT distribution, volume fraction, and exponent degree profoundly influence the buckling behaviour of the respective structures.

Research on multi-functional materials has gained tremendous traction over the last couple of years. Among these, magneto-electro-elastic (MEE) materials have proved beneficial as they can convert energy among three fields-elastic, electric and magnetic. This coupling phenomenon exhibited allows them to be used in different actuators and vibrating structures (Mahesh 2019a, 2020). Mohammadimehr *et al*. (2019) analysed the vibration behaviour of CNT reinforced cylindrical shells made of MEE material. The properties vary by temperature changes, and the governing equations are derived using a variety of fundamental concepts. Mahesh (2019b) developed a finite element formulation to examine the free vibration behaviour of CNTMEE rectangular and skew plates. The change in plate's natural frequency with respect to CNT volume fraction, boundary condition and aspect ratio was studied. Since the material was assumed to be functionally graded, it was observed that the FG-X distribution has the highest stiffness and frequency, thereby, increasing the aspect ratio lowers the plate's frequency. Mahesh and Harursampath (2020a) used the Higher-order shear deformation theory (HSDT) to develop a finite element formulation for the non-

linear vibration behaviour of CNT reinforced MEE plates. Electromagnetic conditions, aspect ratio and CNT arrangement are studied and compared. The impact of coupling fields on non-linear frequency response is also investigated. Ebrahimi *et al*. (2021a) modelled the vibration response of a sandwich plate composed of MEE-FG porous face sheets, along with a CNT reinforced composite core. A refined plate theory based on four-variable shear deformation was used to carry out the analysis. The effect of porosity, FG- distribution and CNT distribution on the vibration response is studied. CNT reinforced shells were studied in different research works (Mahesh and Harursampath 2020b, c), which focused on deflection and non-linear vibration analysis. Mohammadimehr *et al*. (2018) used the FSDT principle to study the vibration behaviour of CNT reinforced MEE cylindrical panels. It was concluded that increasing the CNT volume fraction increases the panel's stiffness; the orientation angle and elastic foundation both substantially impact the system's natural frequency. Rostami and Mohammadimehr (2020) used the DQM to assess the vibration control of sandwich cylindrical shells. The considered configuration consists of CNT reinforced composite face sheets and FG-MEE porous core. The frequency of rotation was determined, and various parametric studies were conducted to investigate the influences of CNT volume fraction, porosity distribution, boundary conditions, temperature etc.

Several recent research papers have focused on functionally graded carbon nanotube-reinforced materials, in which the associated material properties vary according to a mathematical function. The vibration behaviour of a functionally graded CNT reinforced composite plate present in an elevated thermal environment was examined by Mehar *et al*. (2016). Isoparametric elements were used for discretisation, and the results obtained are validated by comparing them with simulation results from ANSYS. FG-X distribution was found to produce the largest stiffness, and it was concluded that the thermal load of the temperature-dependent properties was crucial for the analysis. Thomas and Roy (2016) dealt with the vibration analysis of FG-CNTRC shell structures. According to Mindlin's finite element formulation hypothesis, different shell structures such as spherical, ellipsoidal, and doubly curved were analysed using an eight-noded shell element. Mohammadimehr *et al*. (2017) analysed an MEE sandwich panel using a higher-order sandwich panel and strain gradient theory. It consists of CNT reinforced functionally graded facesheets. The influence of temperature and circuit boundary conditions on the material properties is also studied. Heidari *et al*. (2020) presented an interesting article dealing with the static and buckling analysis of FG-CNTRCs. Here, piezoelectric layers are included within the structure, and the effect of various CNT distributions, aspect ratios, and piezo layers are presented in detail. The work serves as a base for producing more accurate models for FG-CNTRC based structures. Vibration analysis, both linear and non-linear, of different CNT based structures were presented in several research articles (Heshmati Yas 2013, Arami *et al*. 2021, Ebrahimi and Farazmandnia 2017, Thomas and Roy 2017, Mohseni and Shakouri 2019). Mehar *et al*. (2018) depicted the non-linear frequency response of a sandwich panel reinforced with CNT, placed in a uniform temperature field, using an isoparametric finite element method. Tung (2017), in his work, researched the thermal and post-buckling behaviour of FG-CNTRC plates. CPT is used for the formulation after considering von-Karman nonlinearity and Pasternak type foundation interaction. Several articles have evaluated various CNT reinforced composites' static and dynamic analysis (Hajmohammad *et al*. 2017, Mallek *et al*. 2020, Moradi-Dastjerdi *et al*. 2013, Mehar *et al*. 2018).

The comprehensive literature survey revealed that although many research articles have explored CNT reinforced composite structures and CNT based magneto-electro-elastic materials, no work has investigated MEE-CNT based energy harvesting systems. This article aims to bridge this gap and make the first attempt to study CNT reinforced magneto-electro-elastic smart material-based energy harvesting systems. The coupling properties of MEE materials together with CNT reinforcements would enable efficient energy output to be produced. The effect of CNT material parameters and distribution pattern, together with the system's external parameters under consideration, are extensively studied and presented Therefore, the outcome of this article would serve as a benchmark for developing various sustainable energy harvesting solutions by the usage of CNT-reinforced multifunctional composites.

2. Configuration and Material used

2.1 MEE-CNT energy harvester setup

A schematic representation of the proposed configuration for extracting energy using MEE materials is depicted in Fig. 1. The system consists of a cantilever beam with a single layer of MEE-CNT material, together with an isotropic/composite substrate layer below. The geometric parameters of the beam are L, b and h, which represent the overall length, width and total thickness, respectively. In addition, the thickness of the substrate and MEE layer are represented as h_S and h_M, respectively. Narrow electrodes, assumed to be perfectly conductive, are present on the surface of the material. Owing to this, a constant value of generated potential is maintained across the beam length. As there is a dual coupling in place, in addition to the electric potential, a magnetic potential is produced. This is extracted by utilising a coil of 'N' turns wound across the beam. Two external resistances, namely, R_1 and R_2, are included in the circuit by connecting it to the electrodes and the coil. This serves to extract the harvested electric and magnetic power derived from the potentials.

2.2 CNT reinforced MEE material

The excellent mechanical and electromagnetic coupling properties of carbon nanotubes enable their use in different types of structures for various applications. The volume fraction and distribution pattern of CNT would seemingly affect the material properties, and thus, the output

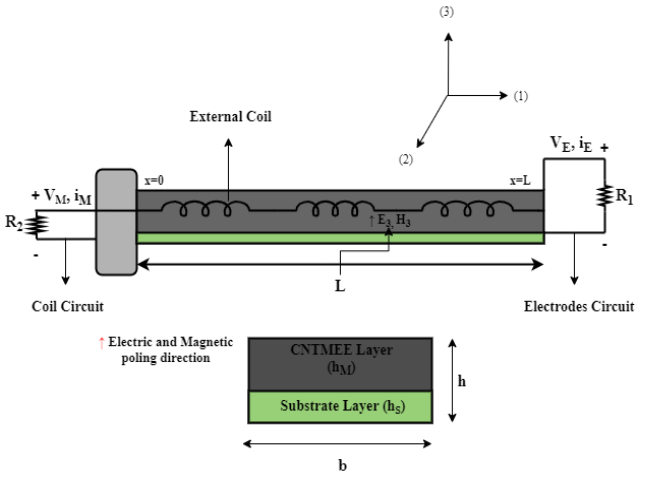

Fig. 1 Schematic representation of MEE-CNT energy harvester

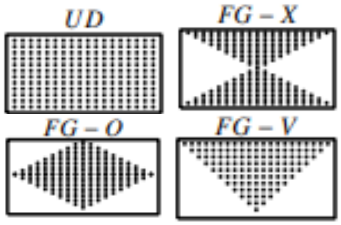

Fig. 2 Representation of CNT distributions

Table 1 Material properties of MEE-CNT material (Mohammadimehr *et al*. 2018)

Material property	Material Constant	SWCNT	PVDF
Elastic constants (GPa)	C_{11}	5825	2.815
Piezoelectric constants (C/m)	e_{31}	0	-0.13
Piezomagnetic constants (N/Am)	q_{31}	22	0
Magneto-electric constant (Ns/VC)	m_{33}	0	-46 x 10^{-12}
Dielectric constant (C^2/Nm^2)	η_{33}	0	0.106 x 10^{-9}
Magnetic permeability (Ns^2/C^2)	μ_{33}	0.25	4 πx 10^{-7}
Density (kg/m^3)	ρ	1400	1780

Table 2 Properties of Substrates

Substrate Material	Young's Modulus (E_{11}) (GPa)	Density (ρ) (kg/m^3)
Aluminium	70	2710
Steel	210	7850
Carbon Epoxy T-300/N5208	10.30	1.60
Aramid Epoxy/ Kevlar 49/Epoxy	5.50	1.46

parameters. These material properties thus need to be investigated to examine the performance of the energy harvesting system. In this system, CNT acts as a piezomagnetic phase and is embedded in the Barium Titanate matrix, which acts as a piezoelectric matrix, to enable coupling between electric, magnetic and elastic fields. Both uniformly distributed and functionally graded distributions are considered (Fig. 2 Mahesh and Harursampath 2020c). The mathematical expressions for volume fraction of CNT are given as:

$$\begin{aligned} &UD; V_{CNT} = V_{CNT}^{*} \\ &FG-X; V_{CNT} = \frac{4|z|}{\hbar} V_{CNT}^{*} \\ &FG-O; V_{CNT} = 2\left(1-\frac{2|z|}{\hbar}\right) V_{CNT}^{*} \\ &FG-V; V_{CNT} = (1+\frac{2|z|}{\hbar}) V_{CNT}^{*} \end{aligned} \tag{1}$$

where, $V_{CNT}^{*} = \frac{w_{CNT}}{w_{CNT}+(\rho_{CNT}/\rho_M)-(\rho_{CNT}/\rho_M)w_{CNT}}$, and w_{CNT} represents the mass fraction of CNT. The pictorial representation of the FG-distributions is shown in Fig. 2.

2.3 Rule of mixture and constitutive equations

The resultant material properties of MEE-CNT can be computed using the Rule of mixtures (Mohammadimehr *et al*. 2018):

$$\begin{aligned} &E_{11} = \eta_{11} V_{CNT} E_{11}^{CNT} + V_m E^m \\ &\frac{\eta_2}{E_{22}} = \frac{V_{CNT}}{E_{22}^{CNT}} + \frac{V_m}{E^m} \\ &\frac{\eta_3}{G_{12}} = \frac{V_{CNT}}{G_{12}^{CNT}} + \frac{V_m}{G^m} \\ &\upsilon_{12} = V_{CNT}\upsilon_{12}^{CNT} + V_m \upsilon^m \\ &\rho = V_{CNT}\rho^{CNT} + V_m \rho^m \end{aligned} \tag{2}$$

here, the superscripts and subscripts 'CNT' and 'm' indicate fiber and matrix, respectively. The efficiency parameters η_1 and η_3 are determined using molecular dynamics simulations. The coupled constitutive equations of MEE-CNT harvester are given as (Vinyas *et al*. 2019)

$$\begin{aligned} &\{\sigma\} = [C]\{\varepsilon\} - [e]\{E\} - [q]\{H\} \\ &\{D\} = [e]^T\{\varepsilon\} + [\eta]\{E\} + [m]\{H\} \\ &B\} = [q]\ \ \{\varepsilon\} + [m]\{E\} + [\mu]\{H\} \end{aligned} \tag{3}$$

here, $[C]$, $[e]$, $[q]$, $[m]$ and $[\mu]$ are the elastic stiffness, piezoelectric, magnetostrictive, electromagnetic, dielectric and magnetic permeability coefficient matrices. $\{\sigma\}$, {D}, and $\{B\}$ represent the stress tensor, electric displacement and magnetic flux respectively and $\{\varepsilon\}$, $\{E\}$ and $\{H\}$ are the linear strain tensor, electric and magnetic field.

The MEE-CNT properties depicted in Eq. (3) can be estimated using the following equations

$$\begin{aligned} &[C] = V_{CNT}[C^{CNT}] + V_m[C^m] \\ &[e] = V_{CNT}[e^{CNT}] + V_m[e^m] \\ &[q] = V_{CNT}[q^{CNT}] + V_m[q^m] \\ &[m] = V_{CNT}[m^{CNT}] + V_m[m^m] \\ &[\eta] = V_{CNT}[\eta^{CNT}] + V_m[\eta^m] \\ &[\mu] = V_{CNT}[\mu^{CNT}] + V_m[\mu^m] \\ &\rho = V_{CNT}\rho^{CNT} + V_m\rho^m \end{aligned} \tag{4}$$

The material properties corresponding to the MEE-CNT and substrate material used in the current study are depicted in Tables 1-2, respectively.

3. Output response modelling

The output parameters of the considered system, quantified by the frequency response functions (FRF's), and their derivation are discussed in this section. For this purpose, a lumped parameter model, having a single degree of freedom, as described in Shirbani *et al*. (2017) is utilised. The representative coupling equations of the MEE-CNT energy harvester is written as follows:

$$M_{eq}\ddot{Z}(t) + C_{eq}\dot{Z}(t) + K_{eq}Z(t) + \theta_{EM}V_E + \theta_{MM}V_M = F(t) \tag{5}$$

$$C_M V_E(t) + \frac{1}{R_1}V_E(t) = \theta_{EM}\dot{Z}(t) + \lambda_{ME}\dot{V}_M \tag{6}$$

$$L_C V_M(t) + R_2 V_M(t) = \theta_{MM}R_2^2\dot{Z} + \lambda_{EM}R_2^2\dot{V}_E \tag{7}$$

The equations depicting the energy balance of the system, considered in the time domain, are given as:

$$\int F\dot{Z}dt = \frac{1}{2}M_{eq}Z^2 + C_{eq}\int \dot{Z}^2\,dt + \frac{1}{2}K_{eq}Z^2 + \int \theta_{EM}V_E\dot{Z}dt + \int \theta_{MM}V_M\dot{Z}dt \tag{8}$$

$$\int (\theta_{EM}\dot{Z}(t) + \lambda_{ME}\dot{V}_M)V_E dt = \int V_E i_E dt + \frac{1}{2}C_M V_E^2 \tag{9}$$

$$\int (\theta_{MM}\dot{Z} + \lambda_{EM}\dot{V}_E)V_M dt = \int V_M i_M dt + \frac{1}{2}\frac{L_C}{R_2^2}V_E^2 \tag{10}$$

As for any vibration-based device, an important parameter on which its design is based is the natural frequency of the system, represented by ω_n, and given by-

$$\omega_n = \sqrt{\frac{K_{eq}}{M_{eq}}} = \sqrt{\frac{25EI}{2(\rho_S h_S + \rho_M h_M)L^3}} \tag{11}$$

The coupling effects produced by the MEE-CNT material, i.e., the stiffness and damping effects produced due to the dual coupling nature of the material (shown in Appendix), tend to have an effect on the natural frequency of the system. The frequency given by Eqn. (11) is modified to include the coupling effects, and is thus given as-

$$\omega_{tr} = \sqrt{\frac{K_{eq} + K_{ele} + K_{mag}}{M_{eq}}} = \omega_n\sqrt{1 + \frac{K_{ele}}{K_{eq}} + \frac{K_{mag}}{K_{eq}}} \tag{12}$$

ω_{tr} is referred to as the true resonant frequency of the system. The true resonant frequency of the system thus models the dynamic behaviour of the system. It is also used while studying the effect of resistances on R_1 and R_2 on the harvester output performance, i.e., $\omega = \omega_{tr}$while varying R_1 and R_2.

As mentioned earlier, the FRF's used to present the output response of the MEE-CNT harvester, namely, normalized displacement, electric and magnetic potential, and total harvested power, are given as:

$$\frac{Z}{\bar{Y}e^{j\omega_a t}} = f_Z = \frac{M_{eq}\omega_a^2}{(K_{eq} + K_{ele} + K_{mag} - M_{eq}\omega_a^2) + j\omega_a(C_{eq} + C_{ele} + C_{mag})} \tag{13}$$

$$\frac{V_E(t)}{\omega_a^2\bar{Y}e^{j\omega_a t}} = \frac{f_{V_E}}{\omega_a^2} \tag{14}$$

$$\frac{V_M(t)}{\omega_a^2\bar{Y}e^{j\omega_a t}} = \frac{f_{V_M}}{\omega_a^2} \tag{15}$$

$$\frac{P_E(t)}{(\omega_a^2\bar{Y}e^{j\omega_a t})^2} = \frac{\left|f_{V_E}\right|^2}{2R_1\omega_a^2} \tag{16}$$

$$\frac{P_M(t)}{(\omega_a^2\bar{Y}e^{j\omega_a t})^2} = \frac{\left|f_{V_M}\right|^2}{2R_2\omega_a^2} \tag{17}$$

$$P_{ME} = P_E + P_M \tag{18}$$

The various lumped parameters and other quantities used to arrive at Eqs. (13) - (18) are shown in Appendix.

4. Numerical results

Here, different parametric studies have been presented to study the influence of material, geometric and external factors on the system's output response. For this purpose, the lumped parameter model discussed in the previous section is utilised. The response of the system is studied by considering all the possible output values that can be obtained: normalized displacement, electric and magnetic voltage, and total extracted power, which is the sum of the electric and magnetic power produced. The prominent material parameters considered for the study include the CNT distribution, CNT volume fraction and the substrate material. External factors like the number of turns of coil and resistance values also form a part of the evaluation.

The mathematical model presented is validated by comparison with published results, and a finite element simulation. The results obtained from Annigeri *et al*. (2007), which present a MEE beam's free vibration behaviour, are recreated using the current mathematical formulation. The results are tabulated in Table 3, which shows good agreement between the values obtained from the MATLAB code and the reference values. Validation of the model incorporating the CNT material properties is done by comparing the output response of the CNTMEE/Al beam with the simulated electric potential value obtained from COMSOL Multi-physics, shown in Fig. 3. This affirms that the formulation can be effectively utilised to study the reinforcement of the MEE material with carbon-nanotubes (CNTs). The output frequency response of the CNTMEE/Al energy harvester is modelled and presented in the following sections. To normalize the results and maintain uniformity, the excitation frequency applied to the base of the beam is presented as a ratio, $\eta = {}^{\omega_a}/_{\omega_n}$, which forms the *x*-axis of the plots.

4.1 Effect of CNT distribution

The influence of CNT distributions, namely, FG-X, FG-V, FG-O and UD, on the output parameters are analysed in Figs. 4(a)-(d). The volume fraction of CNT is considered to be V_f = 0.12. The numerical results reveal that the UD

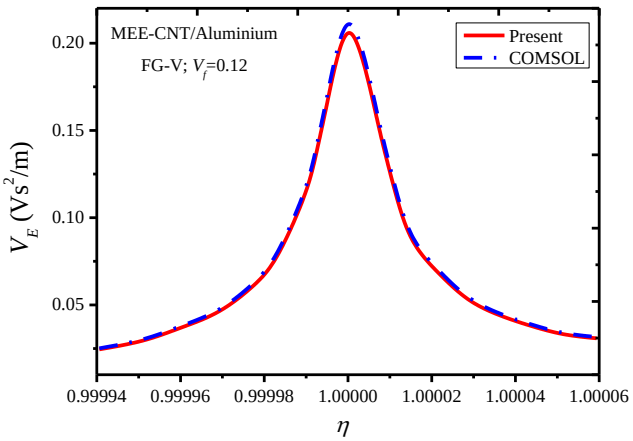

Fig. 3 Validation of the electric potential of MEE-CNT beam

Table 3 Validation studies- free vibration of multiphase MEE beam (V_f = 60% $BaTiO_3$)

Mode number	Annigeri *et al.* (2007)	Present
1	169.97	168.45
2	1043.76	1041.56
3	2835.36	2833.43
4	3902.01	3900.89

Table 4 Effect of volume fraction and FG-Distribution on the output parameters

Various distributions of CNT	Volume fraction of CNT	P_{ME} (x 10^{-4})	V_E	V_M	Z (x 10^8)
UD	0.12	408	7.6292	0.3054	1.4445
	0.17	1399	5.2613	0.5548	1.2366
	0.28	2941	2.8410	0.7840	1.1171
FG-X	0.12	9.3909	0.4255	0.0820	2.0241
	0.17	0.1381	0.0210	0.0482	2.3146
	0.28	8.3660	0.4085	0.0214	2.8026
FG-V	0.12	0.2406	0.0448	0.0530	2.2609
	0.17	3.8312	0.2751	0.0304	2.5866
	0.28	14.0000	0.5287	0.0129	3.1117
FG-O	0.12	73.0000	1.2003	0.1476	1.7402
	0.17	14.0000	0.5163	0.0893	1.9805
	0.28	0.7329	0.1137	0.0416	2.3999

distribution exhibit a predominant influence by producing the highest output power at 0.2941W s^4/ m^2, highest electric potential at 7.6292V s^2/m and highest magnetic potential at 0.7840 V s^2/m. It is followed by FG-O, FG-X and FG-V CNT distributions, and this trend holds good for P_{ME}, V_E and V_M. This trend may be attributed to the uniform and enhanced coupling exhibited by the UD distribution throughout the beam thickness. Meanwhile, for the relative displacement Z, FG-V displays the highest value at 2.2609 x 10^8, and the lowest at 1.1171 x 10^8 is witnessed for UD distribution. This trend is opposite to that observed in the

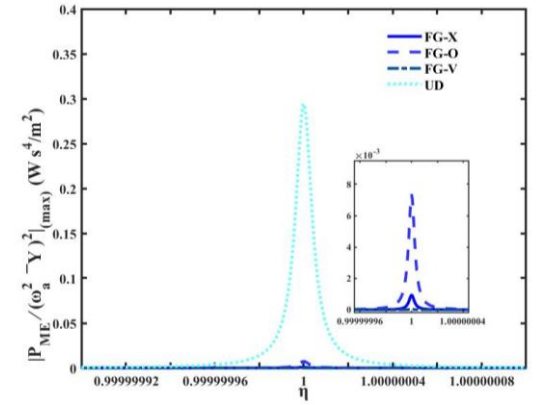

(a) Total harvested power P_{ME}

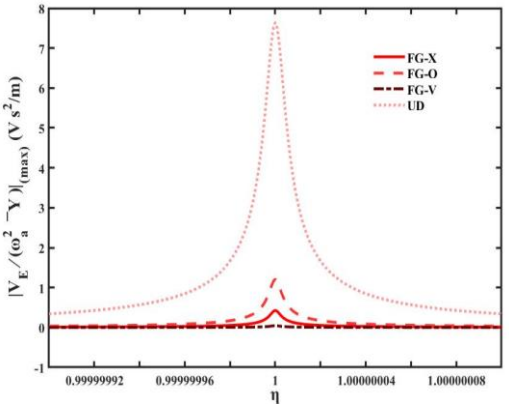

(b) Electric potential V_E

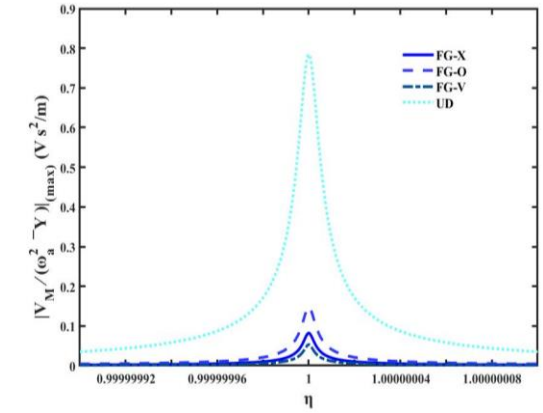

(c) Magnetic potential V_M

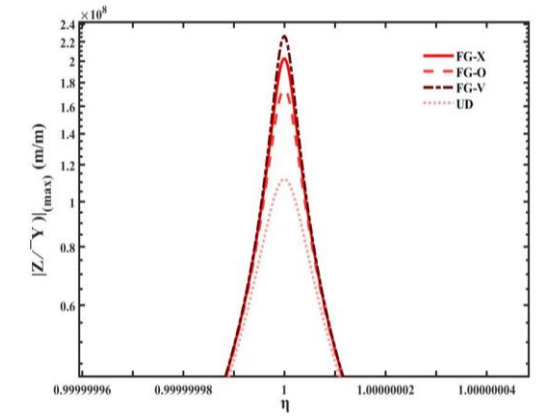

(d) Relative displacement Z

Fig. 4 Effect of CNT distribution

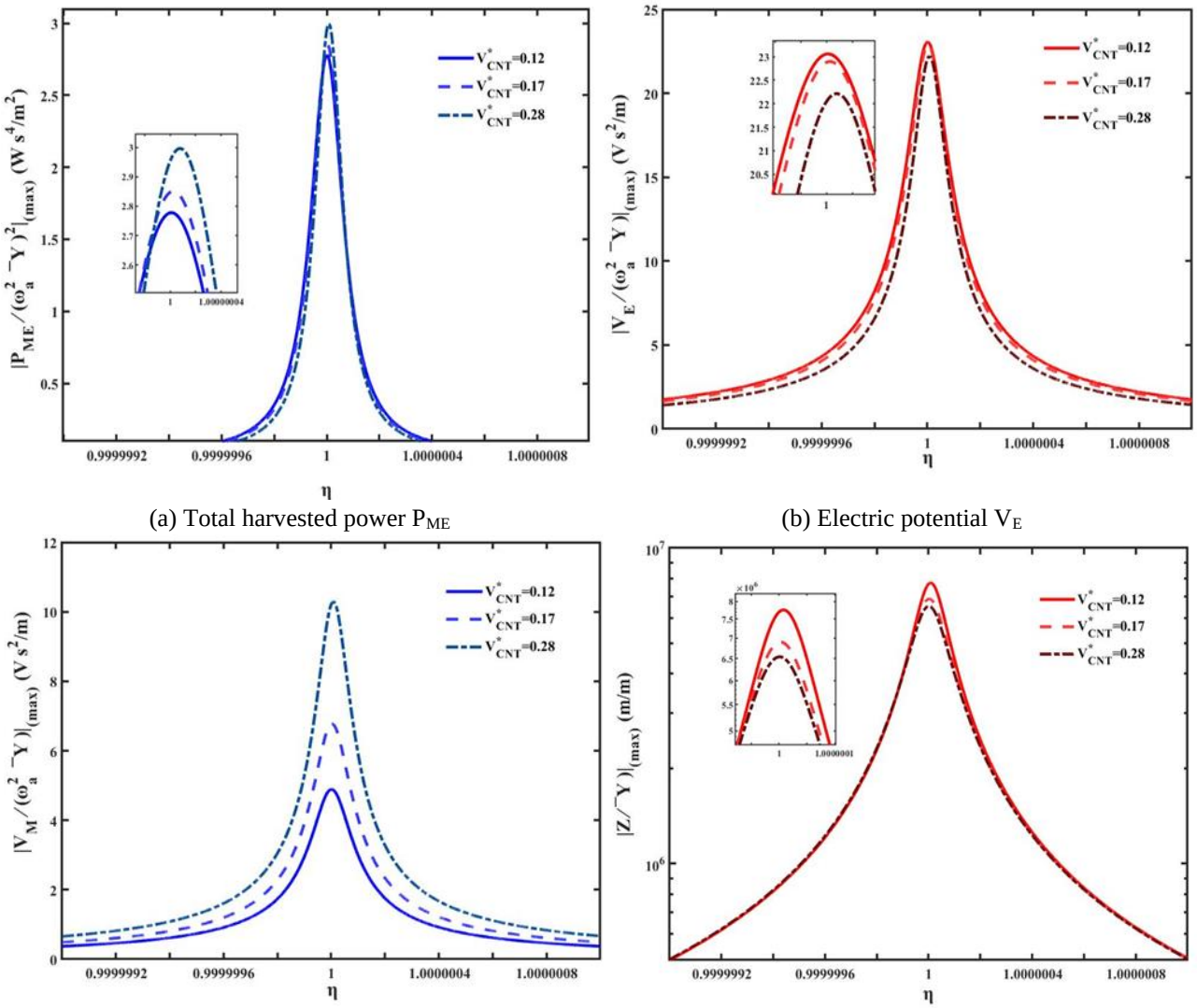

(a) Total harvested power P_{ME}

(b) Electric potential V_E

(c) Magnetic potential V_M

(d) Relative displacement Z

Fig. 5 Effect of CNT volume fraction

other three output parameters. This may be due to the fact that the coupled electromagnetic stiffness and the elastic stiffness of the FG-V distribution are comparatively lesser than the rest of the CNT distributions. The combined effect of volume fraction and functionally graded distribution on the maximum value of various output parameters are shown in Table 4.

4.2 Effect of volume fraction

The effect of CNT volume fractions on the various energy harvester output parameters is studied considering the UD type of CNT distribution. The results corresponding to the output parameters are plotted in Figs. 5(a)-(d). It can be observed that an increase in the volume fraction of CNT increases the overall power produced by the system (Fig. 5(a)). Therefore, V_f = 0.28 has the higher power output, followed by V_f = 0.17 and V_f = 0.12. This can be attributed to the coupling properties associated with the CNT and piezoelectric matrix material. Similar trends are seen for magnetic potential, as depicted in Fig. 5(c). The reason is the higher magnetic coupling generated with higher volume fraction of CNTs which acts as the piezomagnetic phase in the system. A reverse in the trend is observed for electric potential and relative displacement. It is seen that volume fraction V_f = 0.12 produces the highest output value, which decreases with an increase in volume fraction. The lower volume fraction of CNTs refers to the higher volume fraction of the piezoelectric phase. Therefore, increasing the volume fraction of CNTs decreases the amount of piezoelectric material, hence decreasing electrical coupling and electric potential. Meanwhile, piezoelectric phase has a lesser coefficient of stiffness values than that of CNTs. Therefore, the relative displacement is larger for the system with a lower volume fraction of CNTs, i.e., V_f = 0.12.

4.3 Effect of substrate material

The influence of substrate materials on the output parameters is shown in Figs. 6(a)-(d). Here, four different

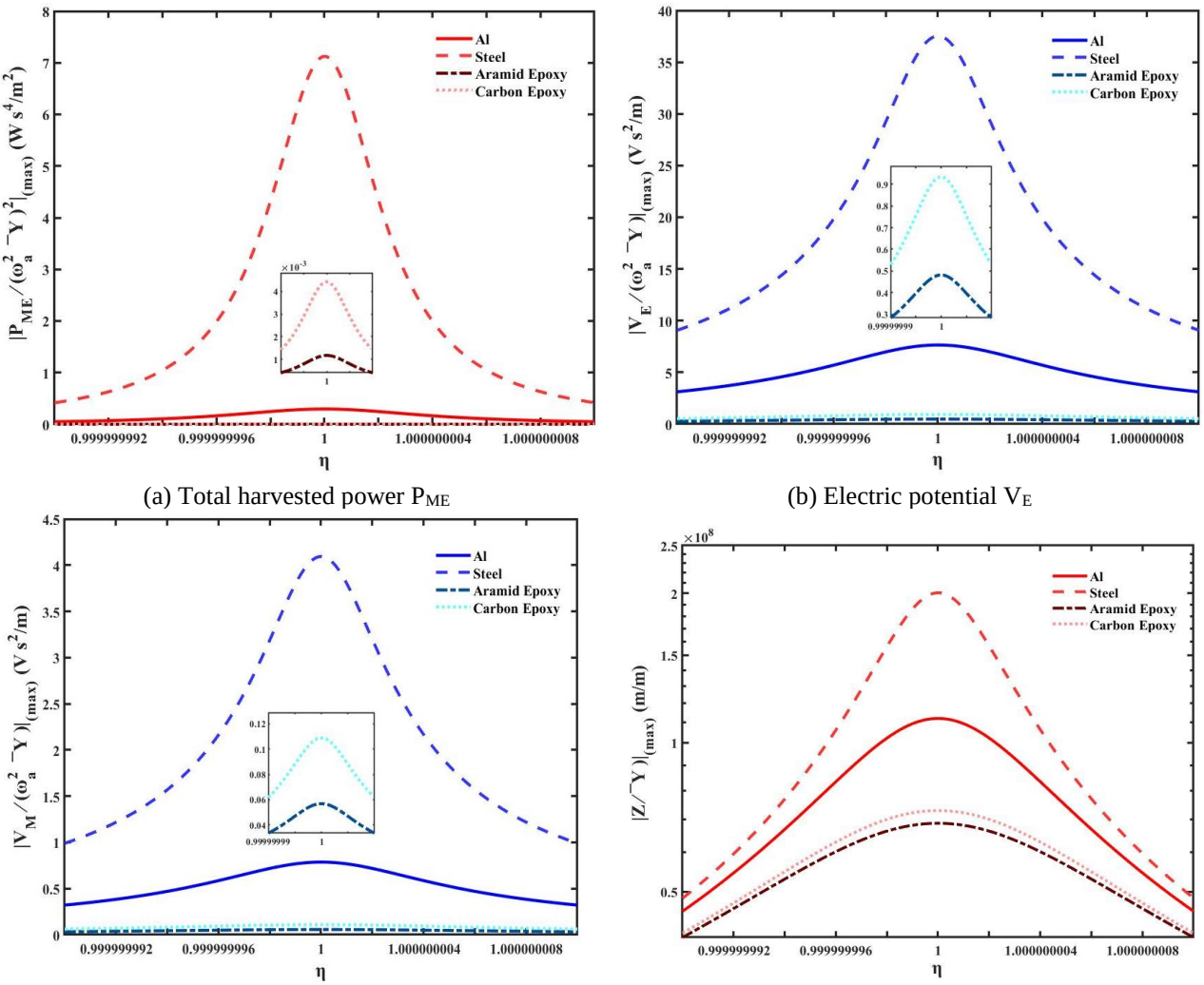

(a) Total harvested power P_{ME}

(b) Electric potential V_E

(c) Magnetic potential V_M

(d) Relative displacement Z

Fig. 6 Effect of substrate material

substrate materials, two isotropic (Aluminium and Steel) and two composite materials (Carbon Epoxy T300 and Aramid Epoxy), are explored. The properties of substrates materials used are shown in Table 2. Since the beam is under transverse excitation, the transverse properties of the composite materials are considered. The computational analysis is carried out for UD type of CNT distributions with volume fraction V_f = 0.12. As seen in Figs. 6(a)-(d), the maximum total harvested power follows the trend Steel > Al > Carbon epoxy > Aramid epoxy. This is attributed to the higher value of Young's modulus of each material. Thus, the type of substrate material used significantly affects the harvester's performance. A similar trend of variation is observed for the other parameters, namely electric potential (Fig. 6(b)), magnetic potential (Fig. 6(c)), and relative displacement (Fig. 6(d)) also.

4.4 Effect of number of turns of coil

The influence of the number coil turns on the frequency response of MEE-CNT energy harvesters is studied in this section. The Figs. 7(a)-(d) show the variation in output values for uniform distribution (UD) of the carbon nanotubes for three different volume fraction (V_f) values. Three distinct values of coil turns N =1, 5 and 10 are considered. The values of resistances R_1 and R_2 are set as $10^2\ \Omega$. It can be observed from these plots that increasing the number of coil turns leads to a decrease in total power P_{ME}, magnetic potential V_M. The reason may be the increase in magnetic stiffness K_{mag} and decrease in magnetic damping C_{mag}. However, an increase in the electric potential V_E and relative displacement Z is observed in Fig. 7(b) and 7(d). This may be attributed to the slight decrease in coupled electrical stiffness K_{ele}, combined with electrical damping C_{ele}, which does not increase with an increase in N. It is also observed that the increase or decrease in output parameters with N is less pronounced as N is increased from 5 to 10, suggesting a saturation effect. The combined effect of the different parameters studied in the above sections has been comprehensively tabulated in Tables 5-8. The effect of varying CNT distributions, volume fraction, substrate materials, and the number of turns on the maximum values maximum values of the output parameters have been considered.

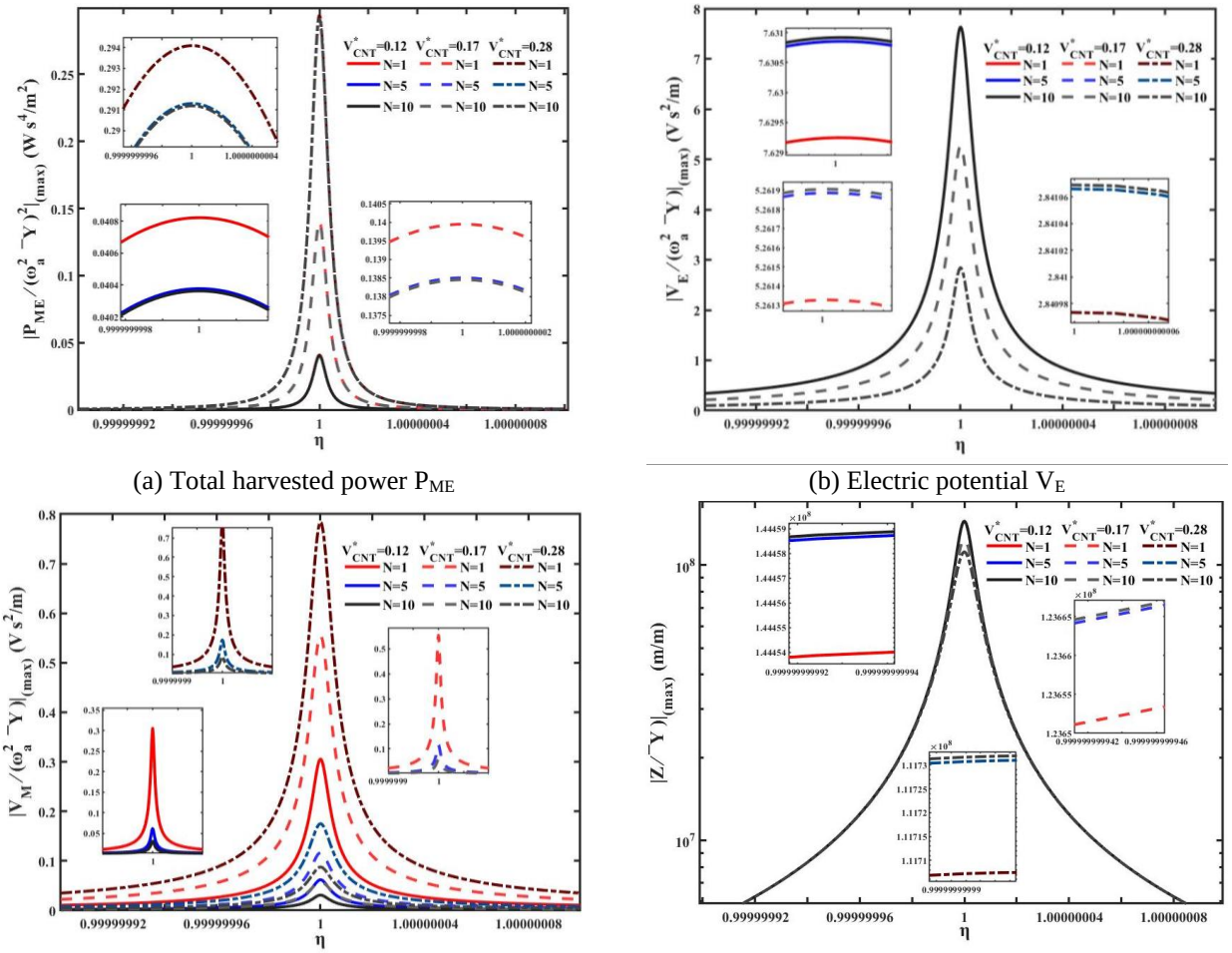

(a) Total harvested power P_{ME}

(b) Electric potential V_E

(c) Magnetic potential V_M

(d) Relative displacement Z

Fig. 7 Effect of number of turns of coil (*N*)

Table 5 Variation of the maximum electrode voltage (V_E) with different combinations of substrates, number of coil turn (*N*), CNT Distribution and volume fraction V_f (R_1=R_2 = 10^2) (V s^2/m)

Substrate	CNT distribution	V_f= 0.12			V_f= 0.17			V_f= 0.28		
		N=1	*N*=5	*N*=10	*N*=1	*N*=5	*N*=10	*N*=1	*N*=5	*N*=10
Aluminium	UD	7.6463	7.6480	7.6482	5.2732	5.2737	5.2738	2.8473	2.8475	2.8476
	FG-X	0.4260	0.4266	0.4268	0.0209	0.0210	0.0211	0.4093	0.4095	0.4096
	FG-O	1.2030	1.2033	1.2035	0.5173	0.5175	0.5176	0.1139	0.1140	0.1141
	FG-V	0.0445	0.0449	0.0451	0.2756	0.2758	0.2759	0.5300	0.5301	0.5302
Steel	UD	37.5207	37.5720	37.5741	28.4787	28.5026	28.5034	16.8129	16.8183	16.8186
	FG-X	2.7474	2.7478	2.7479	0.1387	0.1389	0.1390	2.8263	2.8265	2.8266
	FG-O	7.5175	7.5182	7.5183	3.3201	3.3203	3.3204	0.7581	0.7582	0.7583
	FG-V	0.2950	0.2952	0.2954	1.8645	1.8647	1.8648	3.7916	3.7918	3.7919
Aramid Epoxy	UD	0.4811	0.4813	0.4814	0.3194	0.3197	0.3199	0.1666	0.1667	0.1668
	FG-X	0.0236	0.0238	0.0239	0.0009	0.0011	0.0012	0.0216	0.0218	0.0219
	FG-O	0.0686	0.0687	0.0688	0.0290	0.0292	0.0293	0.0062	0.0063	0.0064
	FG-V	0.0023	0.0024	0.0025	0.0147	0.0149	0.0150	0.0273	0.0274	0.0275
Carbon Epoxy T-300	UD	0.9341	0.9343	0.9344	0.6219	0.6220	0.6221	0.3250	0.3251	0.3252
	FG-X	0.0468	0.0469	0.0470	0.0020	0.0022	0.0023	0.0430	0.0431	0.0432
	FG-O	0.1342	0.1344	0.1345	0.0570	0.0571	0.0572	0.0122	0.0123	0.0124
	FG-V	0.0048	0.0050	0.0051	0.0293	0.0295	0.0295	0.0543	0.0544	0.0545

Table 6 Variation of the maximum coil voltage (V_M) with different combinations of substrates, number of coil turn (N), CNT Distribution and volume fraction V_f (R_1=R_2 = 10^2) (V s^2/m)

Substrate	CNT distribution	V_f= 0.12			V_f= 0.17			V_f= 0.28		
		N=1	N=5	N=10	N=1	N=5	N=10	N=1	N=5	N=10
Aluminium	UD	0.3065	0.0621	0.0311	0.5566	0.1169	0.0584	0.7864	0.1757	0.0879
	FG-X	0.0215	0.0043	0.0021	0.0484	0.0097	0.0048	0.0823	0.0165	0.0082
	FG-O	0.0418	0.0084	0.0042	0.0896	0.0179	0.0090	0.1482	0.0297	0.0149
	FG-V	0.0130	0.0026	0.0013	0.0305	0.0061	0.0031	0.0532	0.0106	0.0053
Steel	UD	2.0832	0.4244	0.2122	3.2825	0.6966	0.3484	4.0936	0.9302	0.4652
	FG-X	0.2098	0.0420	0.0210	0.4280	0.0857	0.0428	0.6827	0.1368	0.0684
	FG-O	0.3759	0.0752	0.0376	0.7353	0.1473	0.0737	1.1361	0.2283	0.1142
	FG-V	0.1357	0.0271	0.0136	0.2855	0.0571	0.0286	0.4651	0.0931	0.0465
Aramid Epoxy (x 10^{-4})	UD	184.000	37.0000	19.0000	372.000	79.0000	40.0000	568.000	132.000	66.000
	FG-X	9.8238	1.9649	0.9824	24.0000	4.7540	2.3770	42.0000	8.4746	4.2373
	FG-O	20.0000	4.0522	2.0261	46.0000	9.2985	4.6493	81.0000	16.0000	8.1030
	FG-V	5.6208	1.1242	0.5620	14.0000	2.8859	1.4429	26.0000	5.2666	2.6333
Carbon Epoxy T-300 (x 10^{-4})	UD	360.000	73.0000	37.0000	720.000	153.000	76.0000	1089.00	252.000	126.000
	FG-X	20.0000	3.9662	1.9831	48.0000	9.5095	4.7548	84.0000	17.0000	8.4327
	FG-O	41.0000	8.1176	4.0588	92.0000	18.0000	9.2449	160.000	32.0000	16.0000
	FG-V	11.0000	2.2868	1.1434	29.0000	5.8004	2.9002	53.0000	11.0000	5.2626

Table 7 Variation of the relative displacement (Z) with different combinations of substrates, number of coil turn (N), CNT Distribution and volume fraction V_f (R_1=R_2 = 10^2) (x10^8)

Substrate	CNT distribution	V_f= 0.12			V_f= 0.17			V_f= 0.28		
		N=1	N=5	N=10	N=1	N=5	N=10	N=1	N=5	N=10
Aluminium	UD	1.4461	1.4462	1.4463	1.2380	1.2382	1.2383	1.1183	1.1186	1.1187
	FG-X	2.8062	2.8064	2.8065	2.3173	2.3174	2.3175	2.0262	2.0265	2.0266
	FG-O	2.4028	2.4030	2.4031	1.9827	1.9828	1.9829	1.7421	1.7423	1.7424
	FG-V	3.1160	3.1162	3.1163	2.5897	2.5898	2.5899	2.2634	2.2636	2.2637
Steel	UD	2.6639	2.6647	2.6649	2.2870	2.2889	2.2891	2.0054	2.0081	2.0083
	FG-X	4.6269	4.6270	4.6271	3.8963	3.8964	3.8965	3.4877	3.4878	3.4879
	FG-O	4.0195	4.0197	4.0198	3.4277	3.4278	3.4279	3.0961	3.0964	3.0965
	FG-V	5.1341	5.1342	5.1343	4.2948	4.2949	4.2950	3.8195	3.8197	3.8198
Aramid Epoxy	UD	1.0108	1.0109	1.0110	0.8036	0.8038	0.8039	0.6870	0.6871	0.6871
	FG-X	2.2147	2.2149	2.2150	1.8113	1.8115	1.8116	1.5560	1.5562	1.5563
	FG-O	1.8845	1.8847	1.8848	1.5168	1.5169	1.5170	1.2953	1.2955	1.2956
	FG-V	2.4484	2.4485	2.4486	2.0406	2.0407	2.0408	1.7650	1.7651	1.7652
Carbon Epoxy T-300	UD	1.0517	1.0519	1.0520	0.8443	0.8446	0.8447	0.7286	0.7288	0.7289
	FG-X	2.2809	2.2810	2.2811	1.8649	1.8651	1.8652	1.6037	1.6039	1.6040
	FG-O	1.9395	1.9398	1.9399	1.5639	1.5641	1.5642	1.3390	1.3391	1.3392
	FG-V	2.5251	2.5253	2.5254	2.1004	2.1007	2.1008	1.8173	1.8175	1.8176

Table 8 Variation of the total harvested power (P_{ME}) with different combinations of substrates, number of coil turn (N), CNT Distribution and volume fraction V_f (R_1=R_2 = 10^2) (W s^4/m^2)

Substrate	CNT distribution	V_f= 0.12			V_f= 0.17			V_f= 0.28		
		N=1	N=5	N=10	N=1	N=5	N=10	N=1	N=5	N=10
Aluminium	UD	410.00	406.00	405.00	1406.0	1391.0	1389.0	2954.00	2926.00	2925.00
	FG-X	8.4097	8.3875	8.3868	0.1391	0.0268	0.0232	9.4364	9.1113	9.1011
	FG-O	0.7368	0.6531	0.6505	14.000	13.000	12.000	73.0000	72.0000	71.0000

Table 8 Continued

Substrate	CNT distribution	V_f= 0.12			V_f= 0.17			V_f= 0.28		
		N=1	*N*=5	*N*=10	*N*=1	*N*=5	*N*=10	*N*=1	*N*=5	*N*=10
Aluminium	14.000	13.000	12.000	3.8507	3.8059	3.8045	0.2421	0.1065	0.1022	14.000
Steel (x 10^{-4})	UD	14351	14152	14144	41091	40644	40628	71228	70626	70602
	FG-X	402.00	400.00	399.00	10.000	1.3318	1.0566	401.000	378.000	377.000
	FG-O	36.000	29.000	28.000	578.00	552.00	550.00	289.000	2829.00	2827.00
	FG-V	720.00	719.00	718.00	178.00	174.00	172.00	15.0000	4.7929	4.4680
Aramid Epoxy (x 10^{-6})	UD	140.67	139.05	139.00	518.00	511.38	511.14	1200.00	1100.00	1000.00
	FG-X	2.3986	2.3940	2.3939	0.0349	0.0078	0.0070	2.9560	2.8700	2.8673
	FG-O	0.2166	0.1969	0.1963	4.3473	4.2437	4.2405	23.9120	23.5990	23.5890
	FG-V	3.7782	3.7767	3.7766	1.1317	1.1217	1.1214	0.0655	0.0323	0.0312
Carbon Epoxy T-300 (x 10^{-5})	UD	UD	53.527	52.905	52.885	200.00	190.00	188.00	440.000	436.000
	FG-X	FG-X	0.9333	0.9314	0.9312	0.0138	0.0030	0.0027	1.1354	1.1013
	FG-O	FG-O	0.0839	0.0760	0.0757	1.6684	1.6275	1.6262	9.1432	9.0206
	FG-V	FG-V	1.4839	1.4832	1.4830	0.4384	0.4343	0.4342	0.0257	0.1246

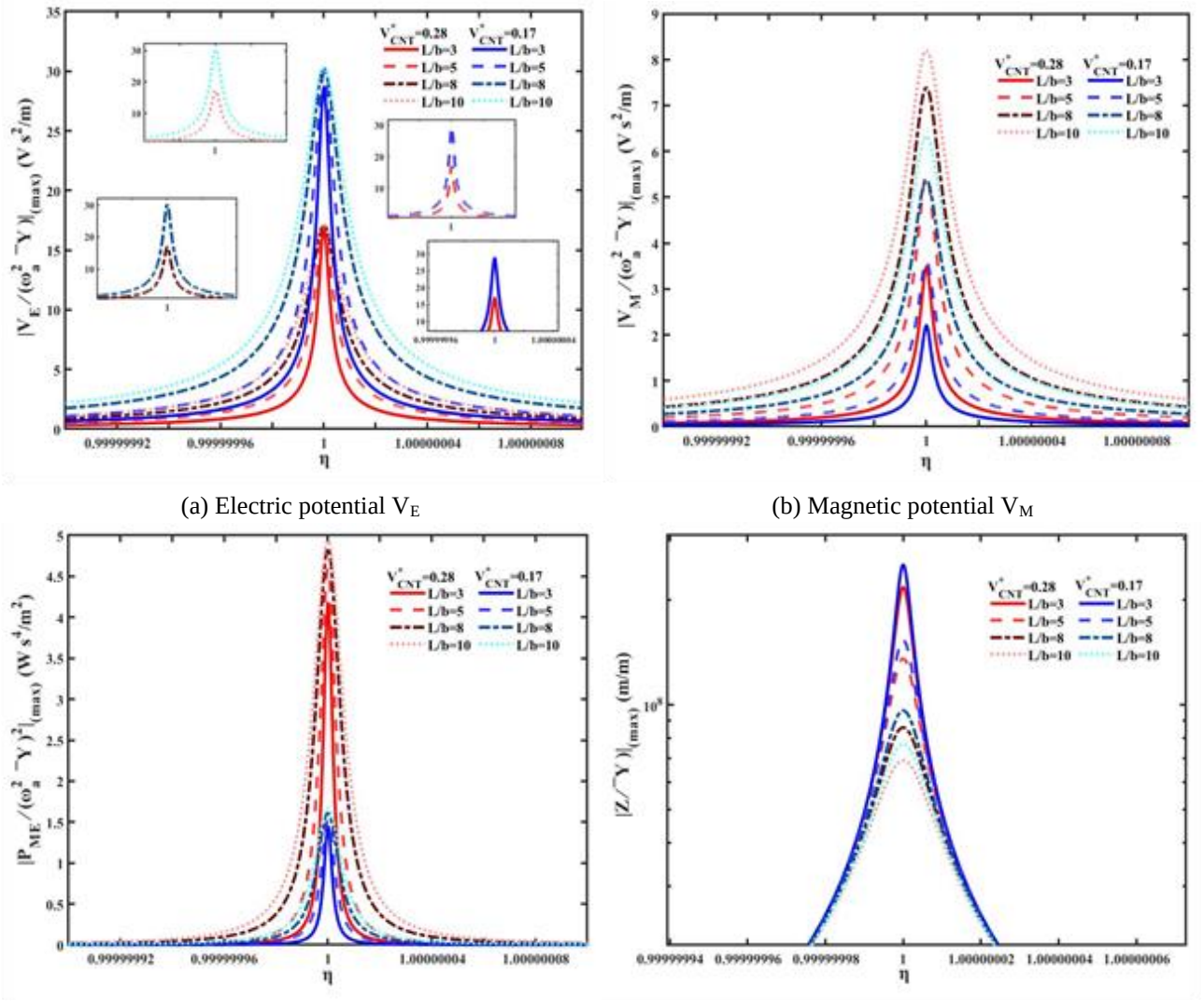

(a) Electric potential V_E

(b) Magnetic potential V_M

(c) Total harvested power P_{ME}

(d) Relative displacement Z

Fig. 8 Effect of *L/b* ratio

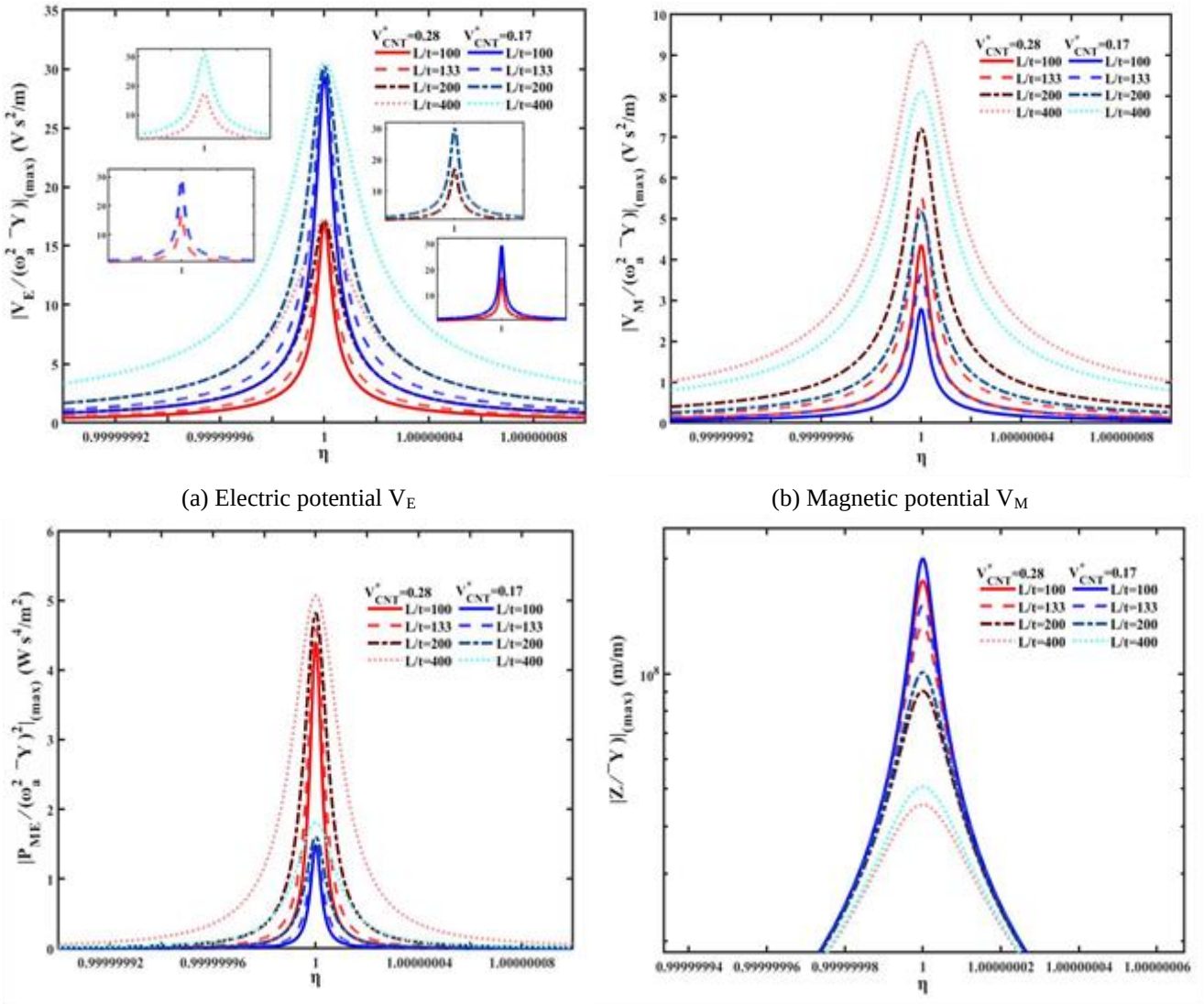

(a) Electric potential V_E

(b) Magnetic potential V_M

(c) Total harvested power P_{ME}

(d) Relative displacement Z

Fig. 9 Effect of *L/t* ratio

4.5 Effect of geometric parameter ratios (L/b and L/t)

The prominent geometric parameters of the system under consideration are length (*L*), breadth (*b*), and thickness (*t*) of the cantilever beam. Fig.'s (8)-(9) represent the variation in the output response of the system as the geometric ratios *L/b* and *L/t* are varied, respectively. As predicted, increasing these ratios improves the electric and magnetic voltage produced, together with the

extracted total power. An increase in *L/b* and *L/t* values also leads to a considerable increase in the equivalent stiffness value, owing to which there is a reduction in the displacement value observed.

4.6 Effect of thickness ratio

The output response variation with substrate to MEE-CNT layer thickness ratio (t_s/t_m) is depicted in Figs. 10(a)-(d). It is observed that there is a decrease in value for all output parameters as the t_s/t_m ratio is increased. An increase in the t_s/t_m ratio suggests that the total percentage of smart MEE-CNT layer in the overall structure reduces. Hence, the degree of coupling attained against the applied base excitation is very less. Thereby, the output parameters reduce.

4.7 Effect of external resistances

This section investigates the influence of electrode and coil resistances R_1 and R_2 on the output parameters. The computation is carried out for UD CNT distribution for a volume fraction V_f = 0.28. Four different values of R_2, namely, 10^0, 10^2, 10^4 and 10^6 Ω, are used. R_1 is varied from 10^0 to $10^{10}\Omega$. The values are computed for a value of N =1. There is no variation seen for V_E and Z, as seen in Figs. 11(a)-(d). For total power P_{ME}, a slight initial variation is observed, which then subsides and combines with the graphs of other values of R_2. For magnetic potential V_M, an increase in the value of R_2 is shown to increase the value of V_M. However, a saturation value is reached beyond R_2=10^4, as the output values for 10^4 and 10^6 coincide.

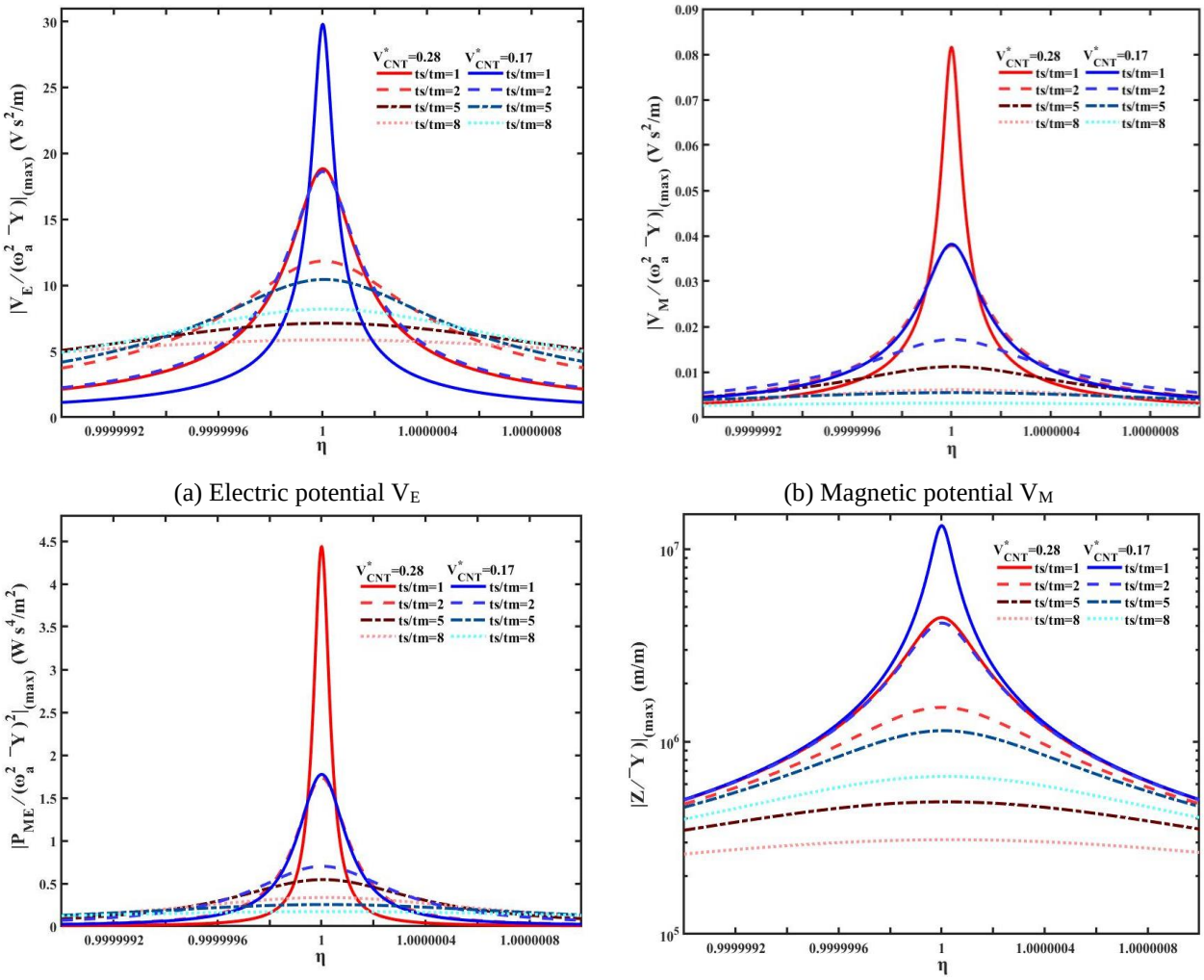

(a) Electric potential V_E (b) Magnetic potential V_M

(c) Total harvested power P_{ME} (d) Relative displacement Z

Fig. 10 Effect of t_s/t_m (thickness ratio)

5. Conclusions

Within this study, the vibration energy harvesting behaviour of the CNT reinforced magneto-electro-elastic cantilever beam is investigated. Special attention is paid to the influence of the reinforcement material of CNT and the effect of its material parameters on the overall energy harvesting output response. For this purpose, the simple and easy to model lumped parameter model is considered. The top layer of the beam consists of a piezoelectric matrix, in which CNT are embedded, which serves as the piezomagnetic phase. The bottom layer consists of an inactive substrate, which can be either an isotropic or composite material. Parametric studies with respect to CNT distribution, volume fraction, substrate material etc., were conducted to assess the variation in the output response. From the results of the numerical studies, the following conclusions can be drawn:

- UD CNT distribution produces the largest output power, followed by FG-O, FG-X and FG-V.
- An increase in volume fraction V_f increases the magnetic potential and output power, but decreases the electric potential and relative displacement produced.
- Steel substrate material results in largest output values, and Aramid epoxy the least.
- An increase in the number of coil turns decreases V_M and P_{ME}, but increases electric potential V_E and relative displacement Z.
- An increase in geometric ratios of the beam such as *L/b* and *L/t* results in an increase in the output parameters.
- Influence of external resistances R_1 and R_2 are shown to be minimal for V_E, Z and P_{ME} and saturate after a particular R_2 value for V_M.

The above results, summarising the effects of various geometric and material parameters, may serve as useful design inputs for vibration-based energy harvesters using multifunctional materials.

Acknowledgments

The financial support by The Royal Society of London through Newton International Fellowship (NIF\R1\212432) is sincerely acknowledged by the authors Vinyas Mahesh and Sathiskumar A Ponnusami.

The financial support by Science and Engineering

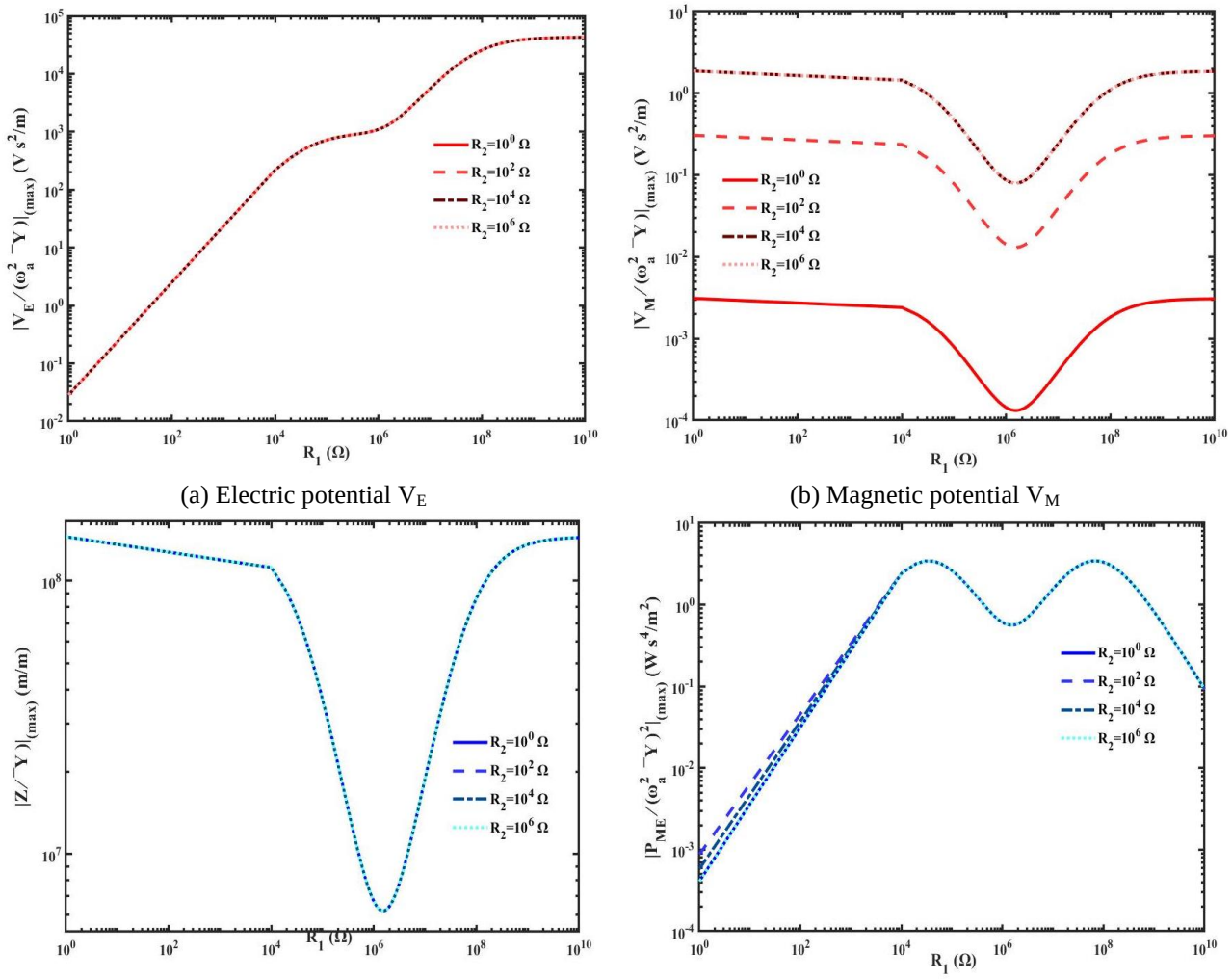

(a) Electric potential V_E (b) Magnetic potential V_M

(c) Relative Displacement Z (d) Total harvested power P_{ME}

Fig. 11 Effect of external resistances R_1 and R_2

for Research Excellence (TAR/2021/000016) is sincerely acknowledged by the authors Vishwas Mahesh and Dineshkumar Harursampath.

References

Allahkarami, F. (2020), "Dynamic buckling of functionally graded multilayer graphene nanocomposite annular plate under different boundary conditions in thermal environment", *Eng. Comput.*, 1-24. https://doi.org/10.1007/s00366-020-01169-7

Annigeri, A.R., Ganesan, N. and Swarnamani, S. (2007), "Free vibration behaviour of multiphase and layered magneto-electro-elastic beam", *J. Sound Vib.*, **299(**1-2**)**, 44-63. https://doi.org/10.1016/j.jsv.2006.06.044

Arani, A.G., Kiani, F. and Afshari, H. (2021), "Free and forced vibration analysis of laminated functionally graded CNT-reinforced composite cylindrical panels", *J. Sandw. Struct. Mater.*, **23**(1), 255-278. https://doi.org/10.1177%2F1099636219830787

Cao, Y., Musharavati, F., Baharom, S., Talebizadehsardari, P., Sebaey, T.A., Eyvazian, A. and Zain, A.M. (2020), "Vibration response of FG-CNT-reinforced plates covered by magnetic layer utilizing numerical solution", *Steel Compos. Struct.*, **37**(2), 253-258. https://doi.org/10.12989/scs.2020.37.2.253

Chen, B., Li, S., Imai, H., Jia, L., Umeda, J., Takahashi, M. and Kondoh, K. (2015), "Load transfer strengthening in carbon nanotubes reinforced metal matrix composites via in-situ tensile tests", *Compos. Sci. Technol.*, **113**, 1-8. https://doi.org/10.1016/j.compscitech.2015.03.009

Ebrahimi, F. and Farazmandnia, N. (2017), "Thermo-mechanical vibration analysis of sandwich beams with functionally graded carbon nanotube-reinforced composite face sheets based on a higher-order shear deformation beam theory", *Mech. Adv. Mater. Struct.*, **24**(10), 820-829. https://doi.org/10.1080/15376494.2016.1196786

Ebrahimi, F., Farazmandnia, N., Kokaba, M.R. and Mahesh, V. (2021a), "Vibration analysis of porous magneto-electro-elastically actuated carbon nanotube-reinforced composite sandwich plate based on a refined plate theory", *Eng. Comput.*, **37**(2), 921-936. https://doi.org/10.1007/s00366-019-00864-4

Ebrahimi, F., Nouraei, M. and Dabbagh, A. (2020), "Thermal vibration analysis of embedded graphene oxide powder-reinforced nanocomposite plates", *Eng. Comput.*, **36**(3), 879-895. https://doi.org/10.1007/s00366-019-00737-w

Ebrahimi, F., Seyfi, A. and Teimouri, A. (2021b), "Torsional vibration analysis of scale-dependent non-circular graphene oxide powder-strengthened nanocomposite nanorods", *Eng. Comput.*, 1-12. https://doi.org/10.1007/s00366-021-01528-y

Eyvazian, A., Musharavati, F., Talebizadehsardari, P. and Sebaey,

T.A. (2020), "Free vibration of FG-GPLRC spherical shell on two parameter elastic foundation", *Steel Compos. Struct.*, **36**(6), 711-727. https://doi.org/10.12989/scs.2020.36.6.711

Farokhian, A. (2020), "The effect of voltage and nanoparticles on the vibration of sandwich nanocomposite smart plates", *Steel Compos. Struct.*, **34**(5), 733-742. https://doi.org/10.12989/scs.2020.34.5.733

Farokhian, A. and Kolahchi, R. (2020), "Frequency and instability responses in nanocomposite plate assuming different distribution of CNTs", *Struct. Eng. Mech.*, **73**(5), 555-563. https://doi.org/10.12989/sem.2020.73.5.555

Ferezghi, Y.S., Sohrabi, M. and Nezhad, S.M.M. (2020), "Meshless Local Petrov-Galerkin (MLPG) method for dynamic analysis of non-symmetric nanocomposite cylindrical shell", *Struct. Eng. Mech.*, **74**(5), 679-698. https://doi.org/10.12989/sem.2020.74.5.679

Ghassabi, M., Zarastvand, M.R. and Talebitooti, R. (2020), "Investigation of state vector computational solution on modeling of wave propagation through functionally graded nanocomposite doubly curved thick structures", *Eng. Comput.*, **36**(4), 1417-1433. https://doi.org/10.1007/s00366-019-00773-6

Gkikas, G., Barkoula, N.M. and Paipetis, A.S. (2012), "Effect of dispersion conditions on the thermo-mechanical and toughness properties of multi walled carbon nanotubes-reinforced epoxy", *Compos. Part B Eng.*, **43**(6), 2697-2705. https://doi.org/10.1016/j.compositesb.2012.01.070

Hajmohammad, M.H., Zarei, M.S., Nouri, A. and Kolahchi, R. (2017), "Dynamic buckling of sensor/functionally graded-carbon nanotube-reinforced laminated plates/actuator based on sinusoidal-visco-piezoelasticity theories", *J. Sandw. Struct. Mater.*, 1099636217720373. https://doi.org/10.1177%2F1099636217720373

Heidari, F., Afsari, A. and Janghorban, M. (2020), "Several models for bending and buckling behaviors of FG-CNTRCs with piezoelectric layers including size effects", *Adv. Nano Res.*, **9**(3), 193-210. https://doi.org/10.12989/anr.2020.9.3.193

Heshmati, M. and Yas, M.H. (2013), "Free vibration analysis of functionally graded CNT-reinforced nanocomposite beam using Eshelby-Mori-Tanaka approach", *J. Mech. Sci. Technol.*, **27**(11), 3403-3408. https://doi.org/10.1007/s12206-013-0862-8

Jagannatham, M., Chandran, P., Sankaran, S., Haridoss, P., Nayan, N. and Bakshi, S.R. (2020), "Tensile properties of carbon nanotubes reinforced aluminum matrix composites: A review", *Carbon*, **160**, 14-44. https://doi.org/10.1016/j.carbon.2020.01.007

Karami, B., Shahsavari, D., Ordookhani, A., Gheisari, P., Li, L. and Eyvazian, A. (2020), "Dynamics of graphene-nanoplatelets reinforced composite nanoplates including different boundary conditions", *Steel Compos. Struct.*, **36**(6), 689-702. https://doi.org/10.12989/scs.2020.36.6.689

Khazaei, P. and Mohammadimehr, M. (2020a), "Vibration analysis of porous nanocomposite viscoelastic plate reinforced by FG-SWCNTs based on a nonlocal strain gradient theory", *Comput. Concr.*, **26**(1), 31-52. https://doi.org/10.12989/cac.2020.26.1.031

Khazaei, P. and Mohammadimehr, M. (2020b), "Size dependent effect on deflection and buckling analyses of porous nanocomposite plate based on nonlocal strain gradient theory", *Struct. Eng. Mech.*, **76**(1), 27-56. https://doi.org/10.12989/sem.2020.76.1.027

Kolahdouzan, F., Mosayyebi, M., Ghasemi, F.A., Kolahchi, R. and Panah, S.R.M. (2020), "Free vibration and buckling analysis of elastically restrained FG-CNTRC sandwich annular nano-plates", *Adv. Nano Res.*, **9**(4), 237-250. https://doi.org/10.12989/anr.2020.9.4.237

Ma, L., Liu, X. and Moradi, Z. (2021), "On the chaotic behavior of graphene-reinforced annular systems under harmonic excitation", *Eng. Comput.*, 1-25. https://doi.org/10.1007/s00366-020-01210-9

Mahesh, V. and Harursampath, D. (2020a), "Nonlinear vibration of functionally graded magneto-electro-elastic higher order plates reinforced by CNTs using FEM", *Eng. Comput.*, 1-23. https://doi.org/10.1007/s00366-020-01098-5

Mahesh, V. and Harursampath, D. (2020b), "Nonlinear deflection analysis of CNT/magneto-electro-elastic smart shells under multi-physics loading", *Mech. Adv. Mater. Struct.*, 1-25. https://doi.org/10.1080/15376494.2020.1805059

Mallek, H., Jrad, H., Wali, M., Kessentini, A., Gamaoun, F. and Dammak, F. (2020), "Dynamic analysis of functionally graded carbon nanotube–reinforced shell structures with piezoelectric layers under dynamic loads", *J. Vib. Control*, **26**(13-14), 1157-1172. https://doi.org/10.1177%2F1077546319892753

Mehar, K., Panda, S.K., Dehengia, A. and Kar, V.R. (2016), "Vibration analysis of functionally graded carbon nanotube reinforced composite plate in thermal environment", *J. Sandw. Struct. Mater.*, **18**(2), 151-173. https://doi.org/10.1177%2F1099636215613324

Mehar, K., Panda, S.K. and Mahapatra, T.R. (2018), "Nonlinear frequency responses of functionally graded carbon nanotube-reinforced sandwich curved panel under uniform temperature field", *Int. J. Appl. Mech.*, **10**(3), 1850028. https://doi.org/10.1142/S175882511850028X

Mehar, K., Panda, S.K. and Mahapatra, T.R. (2017), "Thermoelastic nonlinear frequency analysis of CNT reinforced functionally graded sandwich structure", *Eu. J. Mech. A Solids*, **65**, 384-396. https://doi.org/10.1016/j.euromechsol.2017.05.005

Mohammadimehr, M., Akhavan Alavi, S.M., Okhravi, S.V. and Edjtahed, S.H. (2017), "Free vibration analysis of micro-magneto-electro-elastic cylindrical sandwich panel considering functionally graded carbon nanotube–reinforced nanocomposite face sheets, various circuit boundary conditions, and temperature-dependent material properties using high-order sandwich panel theory and modified strain gradient theory", *J. Intell. Mater. Syst. Struct.*, **29**(5), 863-882. https://doi.org/10.1177%2F1045389X17721048

Mohammadimehr, M., Okhravi, S.V. and Akhavan Alavi, S. (2018), "Free vibration analysis of magneto-electro-elastic cylindrical composite panel reinforced by various distributions of CNTs with considering open and closed circuits boundary conditions based on FSDT", *J. Vib. Control*, **24**(8), 1551-1569. https://doi.org/10.1177%2F1077546316664022

Mohammadimehr, M., Arshid, E., Alhosseini, S.M.A.R., Amir, S. and Arani, M.R.G. (2019), "Free vibration analysis of thick cylindrical MEE composite shells reinforced CNTs with temperature-dependent properties resting on viscoelastic foundation", *Struct. Eng. Mech.*, **70**(6), 683-702. https://doi.org/10.12989/sem.2019.70.6.683

Mohseni, A. and Shakouri, M. (2019), "Vibration and stability analysis of functionally graded CNT-reinforced composite beams with variable thickness on elastic foundation", *J. Mater. Des. Appl.*, **233**(12), 2478-2489. https://doi.org/10.1177%2F1464420719866222

Moradi-Dastjerdi, R., Foroutan, M., Pourasghar, A. and Sotoudeh-Bahreini, R. (2013), "Static analysis of functionally graded carbon nanotube-reinforced composite cylinders by a mesh-free method", *J. Reinforc. Plast. Compos.*, **32**(9), 593-601. https://doi.org/10.1177%2F0731684413476353

Motezaker, M. and Eyvazian, A (2020a), "Buckling load optimization of beam reinforced by nanoparticles", *Struct. Eng. Mech.*, **73**(5), 481-486. https://doi.org/10.12989/sem.2020.73.5.481

Motezaker, M. and Eyvazian, A. (2020b), "Post-buckling analysis

of Mindlin Cut out-plate reinforced by FG-CNTs", *Steel Compos. Struct.*, **34**(2), 289-297. https://doi.org/10.12989/scs.2020.34.2.289
Nazarenko, L., Chirkov, A.Y., Stolarski, H. and Altenbach, H. (2019), "On modeling of carbon nanotubes reinforced materials and on influence of carbon nanotubes spatial distribution on mechanical behavior of structural elements", *Int. J. Eng. Sci.*, **143**, 1-13. https://doi.org/10.1016/j.ijengsci.2019.06.008
Rad, M.H.G., Shahabian, F. and Hosseini, S.M. (2020), "Geometrically nonlinear dynamic analysis of FG graphene platelets-reinforced nanocomposite cylinder: MLPG method based on a modified nonlinear micromechanical model", *Steel Compos. Struct.*, **35**(1), 77-92. https://doi.org/10.12989/scs.2020.35.1.077
Rostami, R. and Mohammadimehr, M. (2020), "Vibration control of rotating sandwich cylindrical shell-reinforced nanocomposite face sheet and porous core integrated with functionally graded magneto-electro-elastic layers", *Eng. Comput.*, 1-14. https://doi.org/10.1007/s00366-020-01052-5
Sahmani, S., Fattahi, A.M. & Ahmed, N.A. (2021) Correction to: "Analytical treatment on the nonlocal strain gradient vibrational response of postbuckled functionally graded porous micro-/nanoplates reinforced with GPL", *Eng. Comput.*, **37**, 793. https://doi.org/10.1007/s00366-020-01009-8
She, G.L. (2020), "Wave propagation of FG polymer composite nanoplates reinforced with GNPs", *Steel Compos. Struct.*, **37**(1), 27-35. https://doi.org/10.12989/scs.2020.37.1.027
Shirbani, M.M., Shishesaz, M., Hajnayeb, A. and Sedighi, H.M. (2017), "Coupled magneto-electro-mechanical lumped parameter model for a novel vibration-based magneto-electro-elastic energy harvesting systems", *Physica E*, **90**, 158-169. https://doi.org/10.1016/j.physe.2017.03.022
Tayeb, T.S., Zidour, M., Bensattalah, T., Heireche, H., Benahmed, A. and Bedia, E.A. (2020), "Mechanical buckling of FG-CNTs reinforced composite plate with parabolic distribution using Hamilton's energy principle", *Adv. Nano Res.*, **8**(2), 135-148. https://doi.org/10.12989/anr.2020.8.2.135
Thomas, B. and Roy, T. (2016), "Vibration analysis of functionally graded carbon nanotube-reinforced composite shell structures", *Acta Mechanica*, **227**(2), 581-599. https://doi.org/10.1007/s00707-015-1479-z
Thomas, B. and Roy, T. (2017), "Vibration and damping analysis of functionally graded carbon nanotubes reinforced hybrid composite shell structures", *J. Vib. Control*, **23**(11), 1711-1738. https://doi.org/10.1177%2F1077546315599680
Tsai, J.L. and Lu, T.C. (2009), "Investigating the load transfer efficiency in carbon nanotubes reinforced nanocomposites", *Compos. Struct.*, **90**(2), 172-179. https://doi.org/10.1016/j.compstruct.2009.03.004
Tung, H.V. (2017), "Thermal buckling and postbuckling behavior of functionally graded carbon-nanotube-reinforced composite plates resting on elastic foundations with tangential-edge restraints", *J. Therm. Stress.*, **40**(5), 641-663. https://doi.org/10.1080/01495739.2016.1254577
Vinyas, M. (2019a), "Vibration control of skew magneto-electro-elastic plates using active constrained layer damping", *Compos. Struct.*, **208**, 600-617. https://doi.org/10.1016/j.compstruct.2018.10.046
Vinyas, M. (2019b), "A higher-order free vibration analysis of carbon nanotube-reinforced magneto-electro-elastic plates using finite element methods", *Compos. Part B Eng.*, **158**, 286-301. https://doi.org/10.1016/j.compositesb.2018.09.086
Vinyas, M. (2020), "Interphase effect on the controlled frequency response of three-phase smart magneto-electro-elastic plates embedded with active constrained layer damping: FE study", *Mater. Res. Exp.*, **6**(12), 125707. https://doi.org/10.1088/2053-1591/ab6649
Vinyas, M. and Harursampath, D. (2020), "Nonlinear vibrations of magneto-electro-elastic doubly curved shells reinforced with carbon nanotubes", *Compos. Struct.*, **253**, 112749. https://doi.org/10.1016/j.compstruct.2020.112749
Vinyas, M., Sunny, K.K., Harursampath, D., Nguyen-Thoi, T. and Loja, M.A.R. (2019), "Influence of interphase on the multi-physics coupled frequency of three-phase smart magneto-electro-elastic composite plates", *Compos. Struct.*, **226**, 11254. https://doi.org/10.1016/j.compstruct.2019.111254
Wang, W., Zhu, Y., Liao, S. and Li, J. (2014), "Carbon nanotubes reinforced composites for biomedical applications", *BioMed Res. Int.*, **2014**. https://doi.org/10.1155/2014/518609
Zare, Y. and Rhee, K.Y. (2020), "Tensile modulus prediction of carbon nanotubes-reinforced nanocomposites by a combined model for dispersion and networking of nanoparticles", *J. Mater. Res. Technol.*, **9**(1), 22-32. https://doi.org/10.1016/j.jmrt.2019.10.025
Zhou, C., Zhan, Z., Zhang, J., Fang, Y. and Tahouneh, V. (2020), "Vibration analysis of FG porous rectangular plates reinforced by graphene platelets", *Steel Compos. Struct.*, **34**(2), 215-226. https://doi.org/10.12989/scs.2020.34.2.215
Zhou, C., Zhao, Y., Zhang, J., Fang, Y. and Habibi, M. (2020), "Vibrational characteristics of multi-phase nanocomposite reinforced circular/annular system", *Adv. Nano Res.*, **9**(4), 295-307. https://doi.org/10.12989/anr.2020.9.4.295
Zerrouki, R., Karas, A. and Zidour, M. (2020), "Critical buckling analyses of nonlinear FG-CNT reinforced nano-composite beam", *Adv. Nano Res.*, **9**(3), 211-220. https://doi.org/10.12989/anr.2020.9.3.211

AT

Appendix

The equivalent SDOF formulations to compute the natural frequency of the MEE cantilever beam, shown in Eqn. (10) are given as-

$$M_{eq} = \frac{24}{100}(\rho_s \hbar_s + \rho_M \hbar_M) bL$$

$$K_{eq} = \frac{3(EI)_{eq}}{L^3}$$

$$EI_{eq} = b[E_T^S[\frac{\hbar_s^3}{12} + \hbar_s(\bar{n} - \frac{\hbar_s}{2})^2] + E_{11}^M[\frac{\hbar_M^3}{12} + \hbar_M(\frac{\hbar_M}{2} + \hbar_S - \bar{n})^2]] \quad \text{(A1)}$$

$$\bar{n} = \frac{\hbar_S^2 + \hbar_M^2 r + 2\hbar_s \hbar_M r}{2(\hbar_s + r\hbar_M)}$$

$$r = \frac{E_T^S}{E_{11}^M}$$

$$\theta_{EM} = -e_{31}^M \frac{b\hbar_{Mc}}{L}$$

$$\hbar_{Mc} = \frac{\hbar_M + 2\hbar_s - 2\bar{n}}{2}$$

$$\theta_{MM} = q_{31}^{M}\frac{Nb\hbar_{Mc}}{R_2 L}$$

$$C_M = \frac{\hbar_{33}^{M} bL}{\hbar_M}$$

$$L_C = \mu_{33}^{M}\frac{N^2 bL}{\hbar_M}$$

$$\lambda_{EM} = \lambda_{ME} = g_{33}^{M}\frac{NbL}{R_2\hbar_M}$$

The various harmonic terms, used to arrive at the FRF's in Eqn.'s (11)- (15) are described as-$V_E = \bar{V}_E e^{j\omega_a t}$, $V_M = \bar{V}_M e^{j\omega_a t}$ and $Z = \bar{Z}e^{j\omega_a t}$ where $\bar{V}_E, \bar{V}_M, \bar{Z}$, represent the amplitudes of generated electric and magnetic voltage and normalized displacement, which are formulated as-

$$\bar{Z} = \frac{M_{eq}\omega_a^2 \bar{Y}}{\left(K_{ele}+K_{eq}+K_{mag}-M_{eq}\omega_a^2\right) + j\omega_a(C_{eq}+C_{ele}+C_{mag})} = f_Z \bar{Y}$$

$$\bar{V}_E = \frac{K_{ele}+j\omega_a C_{ele}}{\theta_{EM}}\bar{Z} = \frac{K_{ele}+j\omega_a C_{ele}}{\theta_{EM}} f_Z \bar{Y} = f_{V_E}\bar{Y} \tag{A2}$$

$$\bar{V}_M = \frac{K_{mag}+j\omega_a C_{mag}}{\theta_{MM}}\bar{Z} = \frac{K_{mag}+j\omega_a C_{mag}}{\theta_{MM}} f_Z \bar{Y} = f_{V_M}\bar{Y}$$

Here, f_{V_E}, f_{V_M}, f_Z, denote the transfer functions based on the generated potentials and normalized displacement values. K_{eq}, K_{ele}, K_{mag}, and C_{eq}, C_{ele}, C_{mag} denote the stiffness and damping terms formed as a result of the coupling effect of the material, given as-

$$K_{ele} = \omega_a \theta_{EM}\, Im(-f_E)$$

$$K_{mag} = \omega_a \theta_{MM}\, Im(-f_M)$$

$$C_{ele} = \theta_{EM}\, Re(f_E)$$

$$C_{mag} = \theta_{MM}\, Re(f_M)$$

The parameters f_E, f_M are given as-

$$f_E = \frac{1}{c_1 + c_2 x_1}$$

$$f_M = \frac{1}{c_3 + c_4 x_2}$$

$$c_1 = \frac{1}{\theta_{EM}}\left(\frac{1}{R_1} + j\omega_a C_M\right)$$

$$c_2 = \frac{-j\omega_a \lambda_{ME}}{\theta_{EM}} \tag{A3}$$

$$c_3 = \frac{R_2 + j\omega_a L_C}{\theta_{MM} R_2^2}$$

$$c_4 = \frac{-j\omega_a \lambda_{EM}}{\theta_{MM}}$$

$$x_1 = \frac{1}{x_2} = \frac{c_1 - c_4}{c_3 - c_2}$$

Finally, the computed values of electric and magnetic power, using the values of the generated electric and magnetic potential and external resistances used, is represented as-

$$P_E = \frac{|V_E^2|}{2R_1} = \frac{\left|f_{V_E}\right|^2 |\bar{Y}|^2}{2R_1} = \frac{|\bar{Y}|^2}{2R_1}\left|\frac{K_{ele}^2 + \omega_a^2 C_{ele}^2}{\theta_{EM}^2}\right|\left|\frac{(M_{eq}\omega_a^2)^2}{(K_{eq}+K_{ele}+K_{mag}-M_{eq}\omega_a^2)^2 + \omega_a{}^2(C_{eq}+C_{ele}+C_{mag})^2}\right| \tag{A4}$$

$$P_M = \frac{|V_M^2|}{2R_2} = \frac{\left|f_{V_M}\right|^2 |\bar{Y}|^2}{2R_2} = \frac{|\bar{Y}|^2}{2R_2}\left|\frac{K_{mag}^2 + \omega_a^2 C_{mag}^2}{\theta_{MM}^2}\right|\left|\frac{(M_{eq}\omega_a^2)^2}{(K_{eq}+K_{ele}+K_{mag}-M_{eq}\omega_a^2)^2 + \omega_a{}^2(C_{eq}+C_{ele}+C_{mag})^2}\right|$$